

Nanoscale Phonon Spectroscopy Reveals Emergent Interface Vibrational Structure of Superlattices

Eric R. Hoglund^{1*}, De-Liang Bao², Andrew O'Hara², Jordan A. Hachtel³, Zachary T. Piontkowski⁴, Joseph R. Matson⁵, Ajay K. Yadav⁶, Ryan C. Haisimaier⁷, Roman Engel-Herbert⁷, Jon F. Ihlefeld¹, Jayakanth Ravichandran⁸, Ramamoorthy Ramesh⁶, Joshua D. Caldwell⁵, Thomas E. Beechem^{4,9}, Sokrates T. Pantelides^{2,10+}, Patrick E. Hopkins^{1,11,12°}, and James M. Howe^{1♦}

¹Dept. of Materials Science and Engineering, University of Virginia, Charlottesville, VA 22904, USA

²Department of Physics and Astronomy, Vanderbilt University, Nashville, TN 37235 USA

³Center for Nanophase Materials Sciences, Oak Ridge National Laboratory, Oak Ridge, TN 37830, USA.

⁴Sandia National Laboratories, Albuquerque, NM 87123, USA

⁵Dept. of Mechanical Engineering and Electrical Engineering, Vanderbilt University, Nashville TN 37235, USA

⁶Dept. of Materials Science and Engineering, University of California Berkley, Berkley, CA 94720, USA

⁷Dept. of Materials Science and Engineering, Pennsylvania State University, University Park, PA, 16802, USA

⁸Dept. of Chemical Engineering and Materials Science, University of Southern California, Los Angeles, CA 90089, USA

⁹Center for Integrated Nanotechnologies, Sandia National Laboratories, Albuquerque, NM, 87123

¹⁰Dept. of Electrical Engineering and Computer Science, Vanderbilt University, Nashville TN 37235, USA

¹¹Dept. of Mechanical and Aerospace Engineering, University of Virginia, Charlottesville, VA 22904, USA

¹²Dept. of Physics, University of Virginia, Charlottesville, VA 22904, USA

*erh3cq@virginia.edu

+pantelides@vanderbilt.edu

°phopkins@virginia.edu

♦jh9s@virginia.edu

1 First paragraph

As the length-scales of materials decrease, heterogeneities associated with interfaces approach the importance of the surrounding materials. Emergent electronic and magnetic interface properties in superlattices have been studied extensively by both experiments and theory.¹⁻⁶

However, the presence of interfacial vibrations that impact phonon-mediated responses, like thermal conductivity ^{7,8}, has only been inferred in experiments indirectly. While it is accepted that intrinsic phonons change near boundaries ^{9,10}, the physical mechanisms and length-scales through which interfacial effects influence materials remain unclear. Herein, we demonstrate the localized vibrational response associated with the interfaces in SrTiO₃-CaTiO₃ superlattices by combining advanced scanning transmission electron microscopy imaging and spectroscopy and density-functional-theory calculations. Symmetries atypical of either constituent material are observed within a few atomic planes near the interface. The local symmetries create local phonon modes that determine the global response of the superlattice once the spacing of the interfaces approaches the phonon spatial extent. The results provide direct visualization and quantification, illustrating the progression of the local symmetries and interface vibrations as they come to determine the vibrational response of an entire superlattice; stated differently, the progression from a material *with* interfaces, to a material *dominated by* interfaces, to a material *of* interfaces as the period decreases. Direct observation of such local atomic and vibrational phenomena demonstrates that their spatial extent needs to be quantified to understand macroscopic behavior. Tailoring interfaces, and knowing their local vibrational response, provides a means of pursuing designer solids having emergent infrared and thermal responses.

2 Introduction

The hierarchy of lattices in superlattices presents a tunable phonon-material interaction where, at small to moderate period thicknesses, coherent and localized interface phonons play a major role in controlling properties. However, it has not been possible so far to probe these excitations with the spatial resolution required to provide knowledge that can ultimately be used for interface engineering and customization of thermal and infrared properties. ^{7,9,11–14} The high spectral and

spatial resolution of monochromated electron energy-loss spectroscopy (EELS) in a scanning transmission electron microscope (STEM) provides a unique opportunity to probe the spatial extent of vibrational excitations that are conventionally assessed by infrared light or neutrons. Such resolving capabilities have so far been demonstrated in resolving phonons associated with chemical changes at point defects and stacking faults in crystals.^{15–18}

Spatially, modern segmented STEM detectors used for integrated differential phase contrast (iDPC) can image both light and heavy elements, providing knowledge of local symmetry, which dictates vibrational properties.^{19–21} Hence, advanced STEM imaging and EELS provides a toolset to understand the intertwined local symmetry and vibrational properties at material interfaces.

In this paper, we combine advanced STEM iDPC and monochromated EELS experiments with density-functional-theory (DFT) calculations to quantify and elucidate the local symmetry and vibrational states in $\text{SrTiO}_3\text{-CaTiO}_3$ (STO-CTO) superlattices. We measure the spatial extent of transient TiO_6 octahedral rotation across STO-CTO interfaces (i.e. octahedral coupling) by quantifying the out-of-phase tilt-angle and relate this information to the local Ti and O vibrational response measured with high-spatial-resolution EELS. DFT calculations are used to model the structural evolution of the superlattices and provide insights into the origins of their differing vibrational properties. The interface vibrations measured using EELS are observed macroscopically with UV-Raman and Fourier Transform Infrared Spectroscopy (FTIR). We show that as the superlattice layer thickness approaches the length scale of octahedral coupling the layers lose uniqueness and adopt the symmetry and vibrational response of the interface. Thus, the vibrational response of the interface becomes more characteristic of the entire material.

3 Results

To evaluate the influence of interfaces, we synthesized three STO-CTO superlattices featuring layer thicknesses of 27, 4, and 2 unit-cells (SL27, SL4, SL2), as shown schematically in Figure 1(a). Large-period SL27 and short-period SL2 were chosen to represent superlattices with well separated and closely spaced interfaces, respectively. SL4 was chosen as an intermediate.

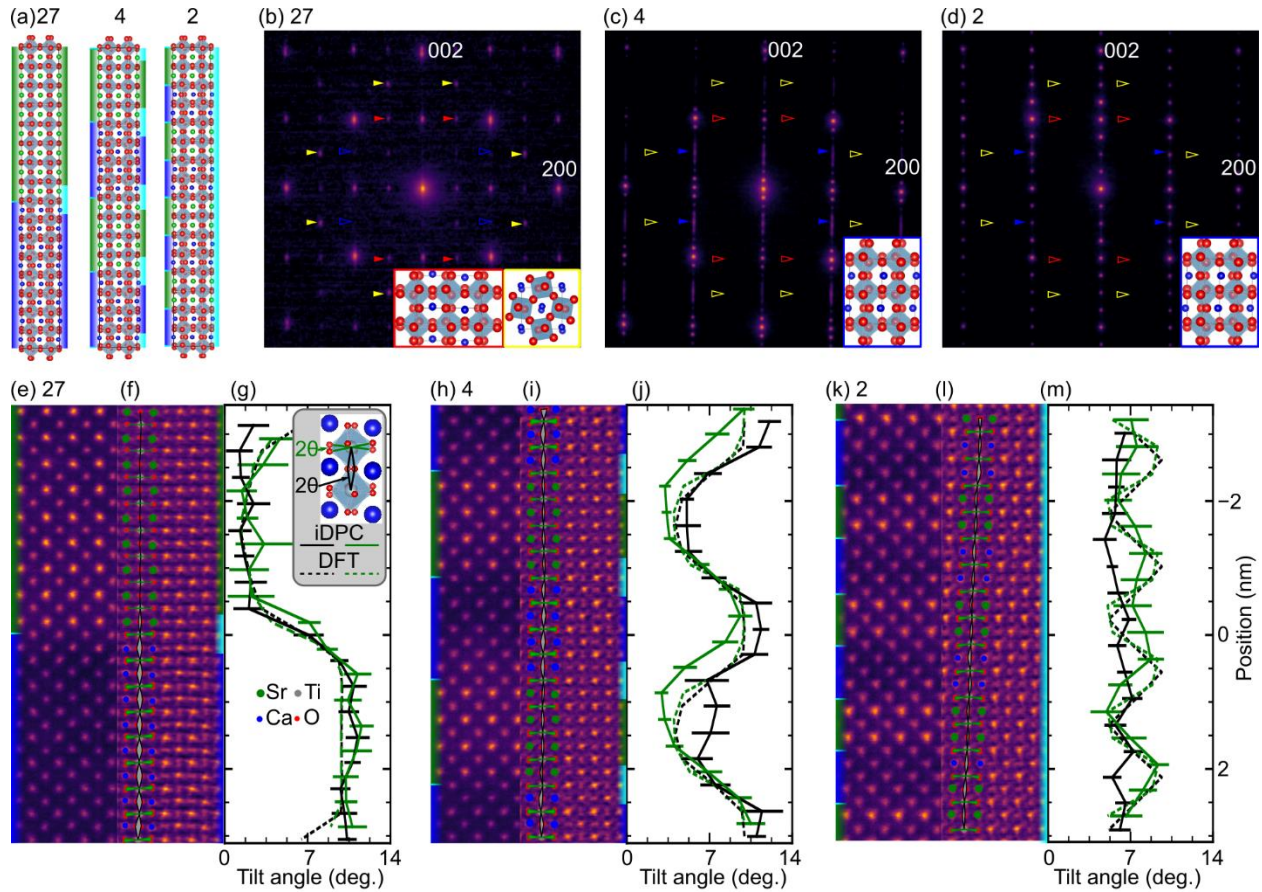


Figure 1. Period dependent changes in the symmetry of STO-CTO superlattices. (a) Superlattices structures calculated from DFT with schematics of the (left) chemically and (right) structurally defined interfaces. Here green, blue, and cyan areas correspond to STO, CTO, and interface layers, respectively; the same colors are used in e,f,h,i,k, and l panels. [100] zone-axis SADP in (b) SL27, (c) SL4, and (d) SL2 grown on NdGaO₃. Yellow, red, and blue arrows correspond to ordered reflections from each of the three possible domains. Solid arrows indicate ordered reflections that exist, and hollow arrows indicate absences. Insets in (b-c) show ball-and-stick models of the domain orientations that are present with border colors matching the arrows they represent. Red and blue arrows and insets are viewed along an out-of-phase tilt-axis and the yellow are viewed along an in-phase tilt-axis. In (c) and (d) superlattice reflections are seen in

the 001 direction. In (b) closely spaced superlattice reflections appear as streaking of the fundamental reflections. (e,h,k) ADF, (f,i,l) iDPC images, and (g,j,m) octahedral tilt-angles of (e-g) SL27, (h-j) SL4, and (k-m) SL2. The legend inside (g) illustrates the (green) in-plane and (black) out-of-plane tilt-angles measured. The tilt-angles for a one unit-cell column are overlaid in each iDPC image to demonstrate the changing in-plane (green triangles) and out-of-plane (grey triangles) tilt-angles. In (g,j,m), solid and dashed curves are from experimental measurements and calculations, respectively. Error bars represent one standard deviation. Chemically abrupt interfaces are illustrated to the left of ADF images (e,h,k) and model structures (a), illustrating the abrupt change between STO (green) and CTO (blue) layers. Chemically diffuse interfaces are illustrated to the right of iDPC images (f,i,l) and model structures (a), illustrating the non-abrupt symmetry changes that are occurring as a result of octahedral coupling.

To quantify the structure of each superlattice, we acquired selected-area electron diffraction patterns (SADP). The SADP reveals that the orientation of octahedral tilts are different in the SL27 structure than are observed in the SL4 and SL2 structures. The large-period SL27 structure exhibits ordered reflections from two of three possible CTO *Pbnm* domains (Figure 1(b)). Both domains have an in-plane *c*-axis as illustrated by the ball-and-stick insets. Different ordered reflections are observed from the SL4 and SL2 samples, indicating a single domain with an out-of-phase *c*-axis (Figure 1(c,d)). The microstructural transition is accompanied by a relaxation of the lattice parameters to a single intermediate value (Figure S3). Thus, as the layer thickness decreases, the underlying crystal structure adapts, resembling a single crystal pattern, which could be enabled by tilting of the TiO₆ octahedra.^{3,4,22–26}

To investigate the potential of such octahedral tilting in the superlattices further, we use annular dark-field (ADF) and iDPC to quantify octahedral tilting (Figure 1(e-m)). The Z-contrast of the ADF images (Figure 1(e,h,k)) allows for discrimination between the brighter Sr and darker Ca atoms and shows chemically abrupt transitions between the two. The phase-contrast of the iDPC images (Figure 1(f,i,l)) allows the measurement of the positions of oxygen and titanium columns, enabling direct quantification of the octahedral tilt angles. In-phase (green triangles) and out-of-

phase (grey triangles) are overlaid on one unit-cell of each iDPC image to demonstrate the changing octahedral tilt-angles from layer-to-layer and structure-to-structure. For example, the iDPC image of SL27 (Figure 1(f)) has three regions defined by observing the splitting of oxygen columns labeled with red circles; 1) single columns in STO, 2) split columns in CTO, and 3) an intermediate splitting at the interface. This result is consistent with simple cubic $Fm\bar{3}m$ STO containing no tilt, orthorhombic $Pbnm$ CTO viewed along an out-of-phase tilt axis, and a coupling region where tilts transition from angles in CTO to none in STO. Scanning convergent-beam electron diffraction corroborates these observations (see Figure S4).

To quantify the observed changes in crystal structure with reduced interface separation, the in-plane and out-of-plane octahedral angles are measured at each site (according to the legend in Figure 1(g)). The average tilt-angle for each horizontal plane is shown in Figures 1(g,j,m) -- see supporting information for complete quantitative values. A coupling region is present at the STO-CTO interface of SL27 (Figure 1(g)), as occurs for in-phase tilt angles in other dissimilar perovskite tilt-systems.^{22–26} We loosely define the structurally diffuse interface width as one unit-cell centered at the chemically abrupt TiO_2 interface (i.e., $\text{SrO}+\text{TiO}_2+\text{CaO}$ planes) as schematically shown in Figure 1(a).

We then turn to SL4 and SL2 to understand how the octahedra couple across the interfaces when the interface spacing is similar to the diffuse interface width. The CTO oxygen column splitting in SL4 is less pronounced than in SL27. Some oxygen columns within the STO layers are distinctly split while most appear elliptical from the partial overlap of the splitting column. The octahedra in STO and CTO are, at some level, coupled through the entire layers seen in the sinusoidal profile of the tilt-angles (Figure 1(j)). Coupling is even more apparent in SL2 (Figure 1(m)), where a nearly constant tilt-angle extends throughout the entire structure.

The changing character of the octahedral coupling observed in Figure 1(g,j,m) can be understood by considering the size of the structurally diffuse interface relative to the period of the superlattice. Enough layers exist in large-period SL27 that interlayer coupling is mitigated, and the material relaxes to something akin to its bulk form. However, for SL4, only two of the four unit-cells are independent from the diffuse interface resulting in coupling extending further into the layers. SL2 pushes this concept to the limit as it contains no unit-cells that are not part of the interface coupling region. A tilt-angle near 7° , which exists only at the interface of the large-period superlattice, is now present throughout the entire superlattice and the structural distinction of each layer has vanished. Therefore, the material is more accurately described as having chemically ordered unit-cells with a single tilt-angle.

Using the STEM results we can define three types of superlattices: (1) Long-period superlattices, such as SL27, exhibit monolithic phases. (2) Moderate-periods (SL4) with modified monolithic phases and structurally diffuse interfaces taking up a sizable fraction of the superlattice. (3) Short-periods (SL2) comprise entirely interface regions and are better described as an ordered structure, having a global symmetry characteristic of that seen at the interfaces of all superlattices. More simply, the short-period superlattice has become a *crystal of interfaces*.

To confirm the observed crystallographic structure of the superlattices and predict the effect of the observed local symmetries on vibrations, we performed DFT calculations on several prototypical superlattice models. We considered long-period (SL8 rather than SL27 owing to computational cost), moderate-period (SL4), and short-period (SL2) models with relaxed atomic structures shown in Figure 1(a). Octahedral tilt angles for both the experimental and theoretical results are in good agreement in both amplitude and periodicity, as indicated by the dashed curves shown in Figure 1(g, j, m). Specifically, SL27 has two bulk-like layers separated by a

structurally diffuse interface. Tilt-angles in SL4 have a sinusoidal profile. SL2 shows the same trend as the experiments, where the structurally diffuse interfaces overlap. It is noteworthy that the calculations show distinguishable oscillations between octahedral tilts in the STO and CTO layers in SL2, whereas the experimental angles appear decoupled from the chemical identity of the planes. This may be caused by finite amounts of intermixing across the interface (Figure S5(a-e)), which is difficult to prevent experimentally, or a metastable phase (Figure S5(g)). From both the structural calculations and experimental measurements, we can conclude that, as the period thickness decreases, the system converges toward a single, emergent structure.

The properties of materials are driven by their underlying crystal symmetry. Thus, changes in this symmetry, as we observed for the moderate and short-period superlattices, modifies superlattice properties. Specifically, the changing symmetry should significantly alter the phonon density of states (DOS), which drive the inherent thermal and infrared optical properties. To evaluate this possibility, we employed DFT to calculate the TiO_3 -projected DOS for each of the three superlattices (Figure 2(a)) (see methods for further description). The DOS shows three peaks: ~ 37 meV (peak 1), ~ 60 meV (peak 2), and ~ 97 meV (peak 3). These modes have energies that correlate with Slater- and Axe-type displacements of the TiO_6 octahedra for a range of perovskites.²⁷ From SL27 to SL4 and SL2, peak 1 red-shifts while peak 3 blue-shifts, indicating an evolution of the superlattice phonon modes as the layer thickness decreases. Thus, vibrational modes assigned to the octahedra change energy as the octahedra they derive from change tilt-angle with decreasing superlattice period thickness.

The attribution of peak shifts to symmetry changes is further supported by comparing the DOS for each constituent layer in the three superlattices (Figure 2(b)). Here, we see that in the SL27 the total DOS for the system (black) deviates from the STO (green), CTO (purple) and interface

(orange) spectra. However, in SL4 in SL2 the total DOS tracks the interface spectrum almost perfectly, illustrating how the interface dominates these shorter-period structures. We can therefore predict that, as the layer thickness decreases, both the structural and vibrational properties converge toward the respective properties of the interfaces.

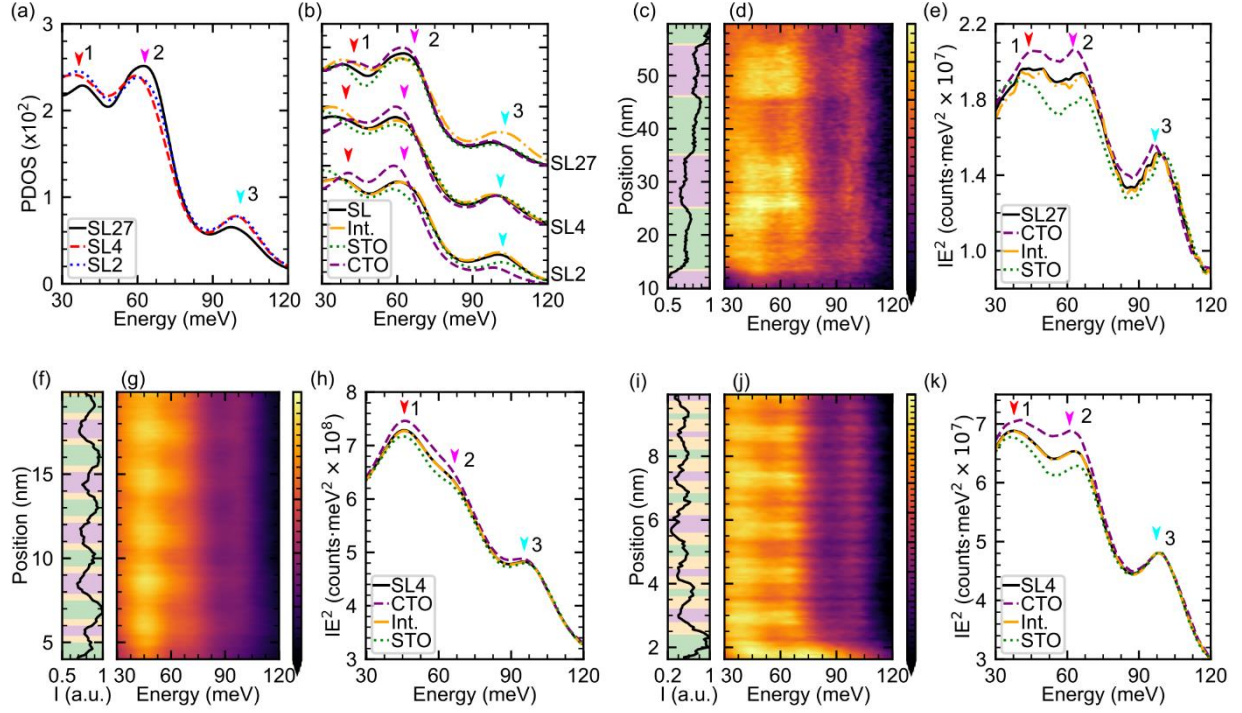


Figure 2. Localized vibrational response of superlattices indicates emergent role of the interfacial symmetry. (a) DFT-calculated phonon DOS of SL27, SL4, and SL2 models. Arrows indicate the dominant phonon peaks. Cascade of (b) DFT-calculated phonon DOS projected on STO (green), CTO (purple), and interface (orange) layers and the total DOS (black) each for superlattice model. (c-k) Monochromated STEM-EELS line profile analyses of the three SL structures: (c-e) SL27, (f-h) SL4, and (i-k) SL2 each with the (c,f,i) ADF profile, (d,g,j) EELS profile, and (e,h,k) integrated spectra from each layer (as indicated by colored regions in the ADF profile).

The evolution in vibrational response of the superlattice is observed directly via spatially resolved off-axis vibrational EELS.^{16,18} With this approach, the difference in vibrational response within the diffuse interface region can be directly compared to that within the

constituent layers themselves. The ADF line profiles of the SL27, SL4, and SL2 are shown in Figure 2(c,f,i), and exhibit a clear distinction between the heavy STO and light CTO layers. The simultaneously acquired EELS are shown in Figure 2(d,g,j). While nominal changes in the local EELS signal are observed, the average responses allow for a direct experimental comparison of the vibrational response of each layer and the entire superlattice. Changes in layer-to-layer response are clearly observed in the superlattices. For example, in SL27 peak 1 is at a lower energy in the STO compared to the CTO, but peaks 2 and 3 are at higher energies, with the interfaces exhibiting intermediate values, demonstrating the capacity to measure the local changes induced from the superlattice symmetries. Furthermore, we note that, while the interface and total-structure spectra bear some similarities, there are features in the interface spectra that cannot be reproduced by a mixture of the bulk-like CTO and STO phases (shown in more detail in supplementary Figure S10(a,b)). Thus, we demonstrate that variations in the localized vibrational spectra are ascribed to the regions of differing symmetry, namely the STO, CTO, and structurally diffuse interface with transient symmetry to the bounding layers.

Like the octahedral-tilt variation, spatial variations in the EELS response reduce with decreasing period. The spectral similarity from layer-to-layer in SL4 relative to SL27 and the exact match between the total and interface spectra indicate that the vibrational state of the superlattice is approaching that of the interface, demonstrating the importance of local vibrational structure as length-scales decrease. The observed response of the superlattice is akin to a crystalline hybrid, where layers hybridize and couple forming new phonons with decreasing layer thickness.^{9,28} The vibrational state of the superlattice approaching that of the interface is further illustrated in SL2. Here, we find practically no layer-to-layer differences in energy between the 3 peaks. The adopted $\text{Ca}_2\text{Sr}_2\text{Ti}_2\text{O}_6$ basis and accompanying symmetry of the SL2 *interface crystal* creates a

material with a global response just like any other periodic crystal. Further demonstration of the convergence of the whole superlattice to an interface-like structure for the moderate- and short-period SLs is shown in Supplementary Figure S10(c-f). The global response of the interface vibrations further demonstrates the importance of local vibrational structure as length-scales decrease.

The question now is: “Do the interface vibrations produce emergent macroscopic responses that cannot be explained as a superposition of the individual constituent layers?” To answer this, UV-Raman and FTIR measurements were undertaken (Figure 3(a-c)).

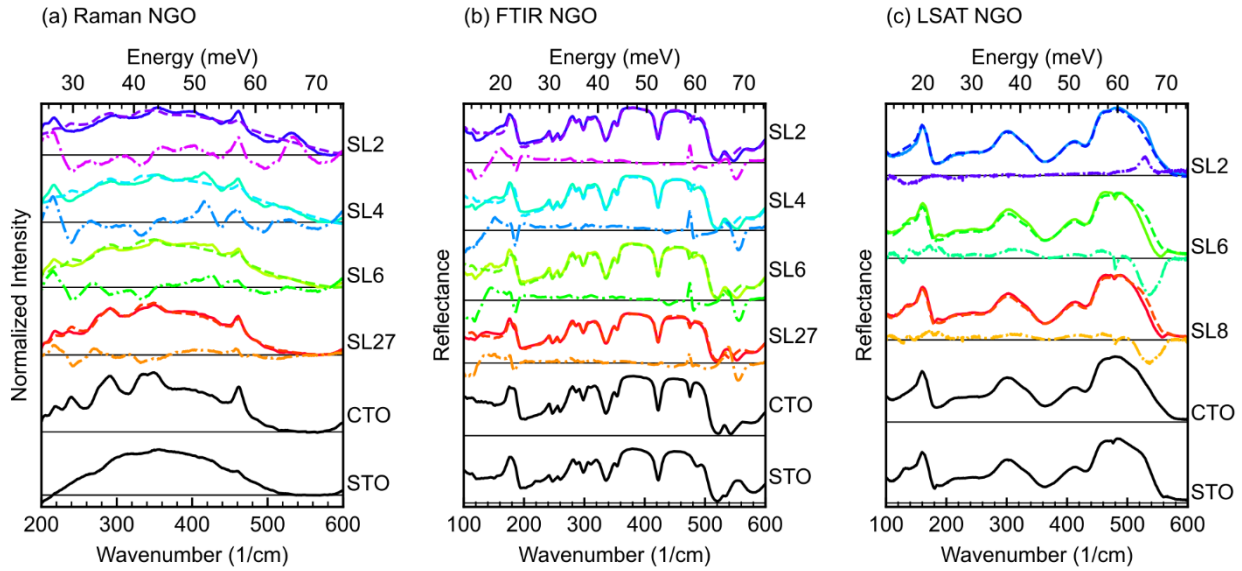


Figure 3. Interface driven modifications in the macroscopic infrared response of STO/CTO superlattices. Raw (solid), fitted (dashed), and residual (dot-dashed) data for (a) UV-Raman and (b) FTIR spectra taken from superlattices on an NGO substrate, and (c) FTIR spectra taken from superlattices on a LSAT substrate. Difference curves are scaled by a factor of two for clarity.

To accentuate the changes that are unique to the superlattice structure, the residual from a fitted linear combination of STO and CTO on substrates is quantified, as shown by dot-dashed lines in Figure 3. With this approach, emergent Raman responses are observed near 220 cm^{-1} (27 meV) and $450\text{-}550\text{ cm}^{-1}$ (60-70 meV) that lessen in intensity as the superlattice period is increased

(Figure 3(a)). A similar evolution is observed in complementary FTIR measurements (Figure 3(b,c)). These emergent modes are similar in energy to that observed on a local level with EELS and that theoretically predicted. We therefore conclude they are a consequence of the alternative symmetry existing at the interfaces of the superlattice. As such, their strength necessarily scales with interface density, resulting in the strongest response for the moderate- (SL4) and short-period (SL2) superlattices. Simply put, there are more interfaces or tilts characteristic of an interface in these films and thus the interfacial signal is stronger. The optical experiments address the question regarding macroscopic response; when the period is reduced to the point where the superlattice takes on the symmetry of the interface, then the localized interface response, directly observed using iDPC and vibrational EELS, is global.

4 Conclusions

From a broader perspective, these results provide an alternative pathway by which nano-structuring can influence material properties. Typically, a superlattice response is thought to arise either through localized or coherent effects. The latter concerns the coherence length of the states with respect to interface periodicity, while for localization, discrete confined quantum states exist that are different than those in the bulk. Neither of these views explain the changes in the vibrational response observed here, because they neglect underlying symmetry changes that can propagate into the constituent materials. When scaling the phases that constitute the material to unit-cell dimensions, the solid takes on a new symmetry that cannot be explained by a combination of the constituent materials. In these STO-CTO superlattices, this new structure results from octahedral coupling between the layers. Here, we have directly imaged these localized changes in symmetry and their impact on vibrations using a combination of STEM iDPC and monochromated EELS, with conclusions drawn supported by DFT. We further

demonstrated how the observed localized phenomena evolve from locally impacting the superlattice at larger periods to dictating the global response of the superlattice as the period decreases. It is important to note that the reported changes in symmetry are not from the global periodicity of the superlattice. Rather, it is the local symmetry changes at the interfaces, and their spatial distribution, that ultimately dictate the entire macroscopic response of the solid as the period thickness decreases. Therefore, tailoring interfaces, and knowing their local response, provides a means of pursuing "designer" solids having emergent infrared and thermal responses not inherent within either of the constituent bulk materials.

5 Methods

5.1 Thin-film growth

Superlattices grown on NdGaO_3 substrates were synthesized using reflection high-energy electron diffraction assisted pulsed laser deposition. Further discussion of growth is found in reference 7 and its supporting information. Superlattices grown on LSAT substrates were realized via molecular beam epitaxy as outlined in reference 29.

5.2 Electron Microscopy

Scanning convergent-beam electron diffraction, ADF and iDPC images were acquired on a Thermo Fisher Themis Z-STEM operating at 300 kV. ADF and iDPC images were acquired with a 30 mrad convergence angle, 200 pA probe current, 625 nm/px dwell time. A 145 mm camera length projected onto the ADF detector with a 200 mrad outer radius and 40 mrad inner radius. The segmented ADF detector used for iDPC had a 38 mrad outer radius and 10 mrad inner radius. The position of metal sites was refined by thresholding, finding the center-of-mass, then

fitting with 2D-Gaussians. The spacing of oxygen columns necessitated locating atomic columns manually.

Vibrational EELS spectra were acquired at 100 keV using a Nion Hermes monochromated aberration-corrected dedicated STEM with a convergence angle of 32 mrad, 25 mrad entrance aperture collection angle, and 0.174 eV/channel dispersions. In this paper, all EELS are acquired in an off-axis mode, obtained by shifting the electron diffraction pattern with respect to EELS entrance aperture. In EELS, delocalized dipole scattering can dominate signals and mask local variations in phonon populations which can be detected by impact scattering. However, by acquiring EELS only from electrons scattered out to high angles, the dipole scattering is reduced more than the impact scattering and the localized signals can be retrieved.^{16,18} Here, we displace the optic axis from the EELS entrance aperture by ~50 mrad in the non-dispersive axis of the spectrometer, and only integrate pixels in the top half of the acquired signal. Thus, the EELS shown in this manuscript has an effective collection semi-angle of ~12.5 mrad that is scattered ~55.5 mrad from the central optic axis.

Vibrational EELS background removal with fitted functions can introduce error because the realistic background does not have a functional shape, due to overlapping of the zero-loss peak and real spectral features such as non-resolvable acoustic or low-energy optic phonons, Therefore, we choose to take an alternate approach normalizing the spectra by multiplying by E^2 thus uniformly normalizing the spectra to a quadratic background. To increase signal-to-noise and compare with theoretical predictions we take the average of all spectra in STO, CTO, and interface layers, akin to layer DOS in DFT. The interface signal is defined as one unit-cell in length for consistency with structural characterization. The layer averaged signals from each layer can then be easily compared to one another and the average superlattice signal. In SL2,

structural characterization showed that we cannot define a structural interface or structurally unique layers. We therefore had three choices; 1) define the entire period as a layer, which is the same as the average superlattice signal and provides no comparable spectra, 2) revert to the definition for chemically defined interfaces, which provides STO and CTO layer average spectra for comparison with each other and the average superlattice signal, or 3) use the structurally diffuse interface width of one unit-cell, which provides the interface, STO, and CTO layer. The third definition does not leave an actual STO or CTO layer, because only a single atomic plane of TiO_2 remains between interfaces. The lack of a complete STO and CTO layer was part of the rationale for a single phase in the iDPC analysis, making choice (3) inconsistent with the structural analysis. Choice (2) would be inconsistent with the EELS analysis of SL27 and SL2. We choose choice (3) so that the EELS analysis between the three superlattices was consistent, and because atomic resolution conditions were not used in the EELS experiments making the one atomic plane delineation of layers infeasible. The lack of spectral change from STO to interface to CTO layer observed in the EELS analysis of SL2 then shows that the layers behave in a similar way, which is consistent with each having a similar symmetry.

5.3 Calculations

The DFT calculations used the Vienna ab initio Simulation Package (VASP)³⁰ with the projected-augmented wave (PAW)^{31,32} method and the local-density-approximation (LDA)³³. The plane-wave basis energy cut off is 600 eV. The superlattice structural models were constructed by alternatively combining *Pbnm*-phase STO and CTO in the *c* direction with specific thicknesses. A SL8 model was chosen to obtain tilt-angles for a large-period superlattice knowing the interface coupling is limited to a few atomic planes, and the prohibitive computational requirements of simulating SL27. For structural relaxation, the structures were

relaxed until the atomic forces were less than 0.01 eV/Å. The lattice parameters were also optimized for each superlattice model. Phonon calculations were performed using the finite-difference method. For structural relaxation and phonon calculations, the k-samplings are 6×6×6 for bulk STO and CTO, 4×4×2 for SL2 and SL4, and 2×2×2 for SL8, respectively. A full width at half maximum (FWHM) of 16 cm⁻¹ was used to plot the projected phonon density of states.

The phonon DOS of each model is obtained by performing weighted average over the respective constituent layers. The projected phonon DOS of a respective constituent layers is averaged to per atom. The total phonon DOS of each model is then obtained by $n_{\text{total}} = (x \times n_{\text{STO}} + y \times n_{\text{CTO}} + z \times n_{\text{int.}})/(x + y + z)$, where x, y, and z are the numbers of atoms considered in each layer. In particular, the phonon DOS of SL27 is obtained by averaging phonon modes of intrinsic bulk STO, intrinsic bulk CTO, and SL8 interface. The interface in all models is defined as one unit-cell on either side of the chemically defined interface, which is consistent with experimental and calculated structures. Since the primary structural changes are associated with TiO₆ octahedra, we can assume that the distinct phonon properties of different superlattices are primarily contributed by Ti/O-related vibrational modes. Therefore, we project the phonon DOS on Ti and O atoms, emphasizing the symmetry-phonon relation. Because only the phonon modes parallel to fields are activated, the phonon DOS is also projected in the (110) plane that is perpendicular to the electron beam.

5.4 Optical Spectroscopies

Raman spectroscopy was performed on samples synthesized atop NGO with a Horiba LabRam Raman instrument employing a 325 nm laser focused using a 40X/0.5 NA objective. Laser powers were verified to be inconsequential to the results. At this wavelength, the skin depth for the exciting UV-light is 26 nm within STO while being >1 μm for CTO. Despite the

transparency of CTO, all Raman examined films were 200 nm in thickness and thus contain at least 100 nm of STO. This is more than 3 times the skin depth and thus the underlying NGO does not impact the Raman experiment. The monolithic samples exhibit a response expected from their bulk form.^{34–38} Raman and FTIR spectra were fitted using a least-squares minimized linear combination of acquired monolithic spectra. This extenuated differences between the superlattice and constituent materials and helped remove the substrate response in the FTIR.

6 References

1. Zhao, W. *et al.* Direct imaging of electron transfer and its influence on superconducting pairing at FeSe/SrTiO₃ interface. *Science Advances* **4**, eaao2682 (2018).
2. Chen, Y. Z. *et al.* Extreme mobility enhancement of two-dimensional electron gases at oxide interfaces by charge-transfer-induced modulation doping. *Nature Mater* **14**, 801–806 (2015).
3. Domínguez, C. *et al.* Length scales of interfacial coupling between metal and insulator phases in oxides. *Nat. Mater.* **19**, 1182–1187 (2020).
4. Moon, E. J. *et al.* Effect of Interfacial Octahedral Behavior in Ultrathin Manganite Films. *Nano Lett.* **6** (2014).
5. Balachandran, P. V. Massive band gap variation in layered oxides through cation ordering. *NATURE COMMUNICATIONS* **7** (2015).
6. Aguado-Puente, P. & Junquera, J. Structural and energetic properties of domains in PbTiO₃/SrTiO₃ superlattices from first principles. *Phys. Rev. B* **85**, 184105 (2012).

7. Ravichandran, J. *et al.* Crossover from incoherent to coherent phonon scattering in epitaxial oxide superlattices. *Nature Materials* **13**, 168–172 (2014).
8. Luckyanova, M. N. *et al.* Coherent Phonon Heat Conduction in Superlattices. **338**, 5 (2012).
9. Ratchford, D. C. *et al.* Controlling the Infrared Dielectric Function through Atomic-Scale Heterostructures. *ACS Nano* **13**, 6730–6741 (2019).
10. Paudel, T. R. & Lambrecht, W. R. L. Computational study of phonon modes in short-period AlN/GaN superlattices. *PHYSICAL REVIEW B* **7**.
11. Koh, Y. K., Cao, Y., Cahill, D. G. & Jena, D. Heat-Transport Mechanisms in Superlattices. *Adv. Funct. Mater.* **19**, 610–615 (2009).
12. Simkin, M. V. & Mahan, G. D. Minimum Thermal Conductivity of Superlattices. *Phys. Rev. Lett.* **84**, 927–930 (2000).
13. Venkatraman, K., Rez, P., March, K. & Crozier, P. A. The influence of surfaces and interfaces on high spatial resolution vibrational EELS from SiO₂. *Microscopy* **67**, i14–i23 (2018).
14. Li, Y.-H. *et al.* Probing lattice vibrations at SiO₂/Si surface and interface with nanometer resolution. *Chinese Phys. Lett.* **36**, 026801 (2019).
15. Yan, X. *et al.* Single-defect phonons imaged by electron microscopy. *Nature* **589**, 65–69 (2021).

16. Hage, F. S., Radtke, G., Kepaptsoglou, D. M., Lazzeri, M. & Ramasse, Q. M. Single-atom vibrational spectroscopy in the scanning transmission electron microscope. *Science* **367**, 1124–1127 (2020).
17. Venkatraman, K., Levin, B. D. A., March, K., Rez, P. & Crozier, P. A. Vibrational spectroscopy at atomic resolution with electron impact scattering. *Nat. Phys.* (2019) doi:10.1038/s41567-019-0675-5.
18. Hage, F. S., Kepaptsoglou, D. M., Ramasse, Q. M. & Allen, L. J. Phonon Spectroscopy at Atomic Resolution. *Physical Review Letters* **122**, 016103–5 (2019).
19. Lazić, I., Bosch, E. G. T. & Lazar, S. Phase contrast STEM for thin samples: Integrated differential phase contrast. *Ultramicroscopy* **160**, 265–280 (2016).
20. de Graaf, S., Momand, J., Mitterbauer, C., Lazar, S. & Kooi, B. J. Resolving hydrogen atoms at metal-metal hydride interfaces. *Sci. Adv.* **6**, eaay4312 (2020).
21. Zheng, Q. *et al.* Direct visualization of anionic electrons in an electride reveals inhomogeneities. *Sci. Adv.* **7**, eabe6819 (2021).
22. Biegalski, M. D. *et al.* Impact of symmetry on the ferroelectric properties of CaTiO₃ thin films. *Appl. Phys. Lett.* **106**, 162904–15 (2015).
23. Aso, R., Kan, D., Shimakawa, Y. & Kurata, H. Atomic level observation of octahedral distortions at the perovskite oxide heterointerface. *Sci Rep* **3**, 2214–6 (2013).
24. Rondinelli, J. M. & Spaldin, N. A. Substrate coherency driven octahedral rotations in perovskite oxide films. *Phys. Rev. B* **82**, 113402 (2010).

25. He, Q. *et al.* Towards 3D Mapping of BO_6 Octahedron Rotations at Perovskite Heterointerfaces, Unit Cell by Unit Cell. *ACS Nano* **9**, 8412–8419 (2015).
26. Middey, S. *et al.* Epitaxial strain modulated electronic properties of interface controlled nickelate superlattices. *Phys. Rev. B* **98**, 045115–8 (2018).
27. Dwij, V. *et al.* Revisiting 70 years of lattice dynamics of BaTiO_3 : Combined first principle and experimental investigation. 16.
28. Caldwell, J. D. *et al.* Atomic-scale photonic hybrids for mid-infrared and terahertz nanophotonics. *Nature Nanotech* **11**, 9–15 (2016).
29. Haislmaier, R. C. *et al.* Overlapping growth windows to build complex oxide superlattices. *APL Materials* **6**, 111104 (2018).
30. Kresse, G. & Furthmüller, J. Efficient iterative schemes for *ab initio* total-energy calculations using a plane-wave basis set. *Phys. Rev. B* **54**, 11169–11186 (1996).
31. Blöchl, P. E. Projector augmented-wave method. *Phys. Rev. B* **50**, 17953–17979 (1994).
32. Kresse, G. & Joubert, D. From ultrasoft pseudopotentials to the projector augmented-wave method. *Phys. Rev. B* **59**, 1758–1775 (1999).
33. Perdew, J. P. & Zunger, A. Self-interaction correction to density-functional approximations for many-electron systems. *Phys. Rev. B* **23**, 5048–5079 (1981).
34. McMillan, P. & Ross, N. The Raman spectra of several orthorhombic calcium oxide perovskites. *Phys Chem Minerals* **16**, (1988).
35. Schaufele, R. F. & Weber, M. J. First- and Second-Order Raman Scattering of SrTiO_3 . *The Journal of Chemical Physics* **46**, 2859–2861 (1967).

36. Hirata, T., Ishioka, K. & Kitajima, M. Vibrational Spectroscopy and X-Ray Diffraction of Perovskite Compounds $\text{Sr}_{1-x}\text{M}_x\text{TiO}_3$ ($\text{M} = \text{Ca}, \text{Mg}$; $0 \leq x \leq 1$). *J. Solid State Chem.* **124**, 353–359 (1996).
37. Balachandran, U. & Eror, N. G. Laser-induced Raman scattering in calcium titanate. *Solid State Communications* **44**, 815–818 (1982).
38. Zheng, H. *et al.* Raman spectroscopy of CaTiO_3 -based perovskite solid solutions. *J. Mater. Res.* **19**, 8 (2004).
39. Nord, M. *et al.* Atomic resolution HOLZ-STEM imaging of atom position modulation in oxide heterostructures. *Ultramicroscopy* **226**, 113296 (2021).

Acknowledgements

ERH and PEH appreciate support from the Office of Naval Research through a MURI Program, Grant Number N00014-18-1-2429. Theory at Vanderbilt University was supported by the U.S. Department of Energy, Office of Science, Basic Energy Sciences, Materials Science and Engineering Directorate grant No. DE-FG02-09ER46554 and by the McMinn Endowment. Calculations were performed at the National Energy Research Scientific Computing Center (NERSC), a U.S. Department of Energy Office of Science User Facility located at Lawrence Berkeley National Laboratory, operated under Contract No. DE-AC02-05CH11231.

Author Contributions

E.R.H., J.A.H., and J.M.H. contributed to the acquisition, analysis, and understanding of all scanning electron microscopy data. D.B., A.O., and S.T.P contributed all density-functional-

theory calculations. Z.P. and T.E.B. contributed acquisition, analysis, and understanding of UV-Raman data. J.R.M, T.E.B, and J.D.C. contributed acquisition, analysis, and understanding of Fourier-transform Infrared spectroscopy data. A.K.Y., R.C.H., R.E.H, J.R., and R.R. contributed growth expertise and samples used in the analysis. J.F.I and P.E.H. contributed an understanding of how the crystal and vibrational structure impacted broader material properties.

S1 Supplemental: Diffraction

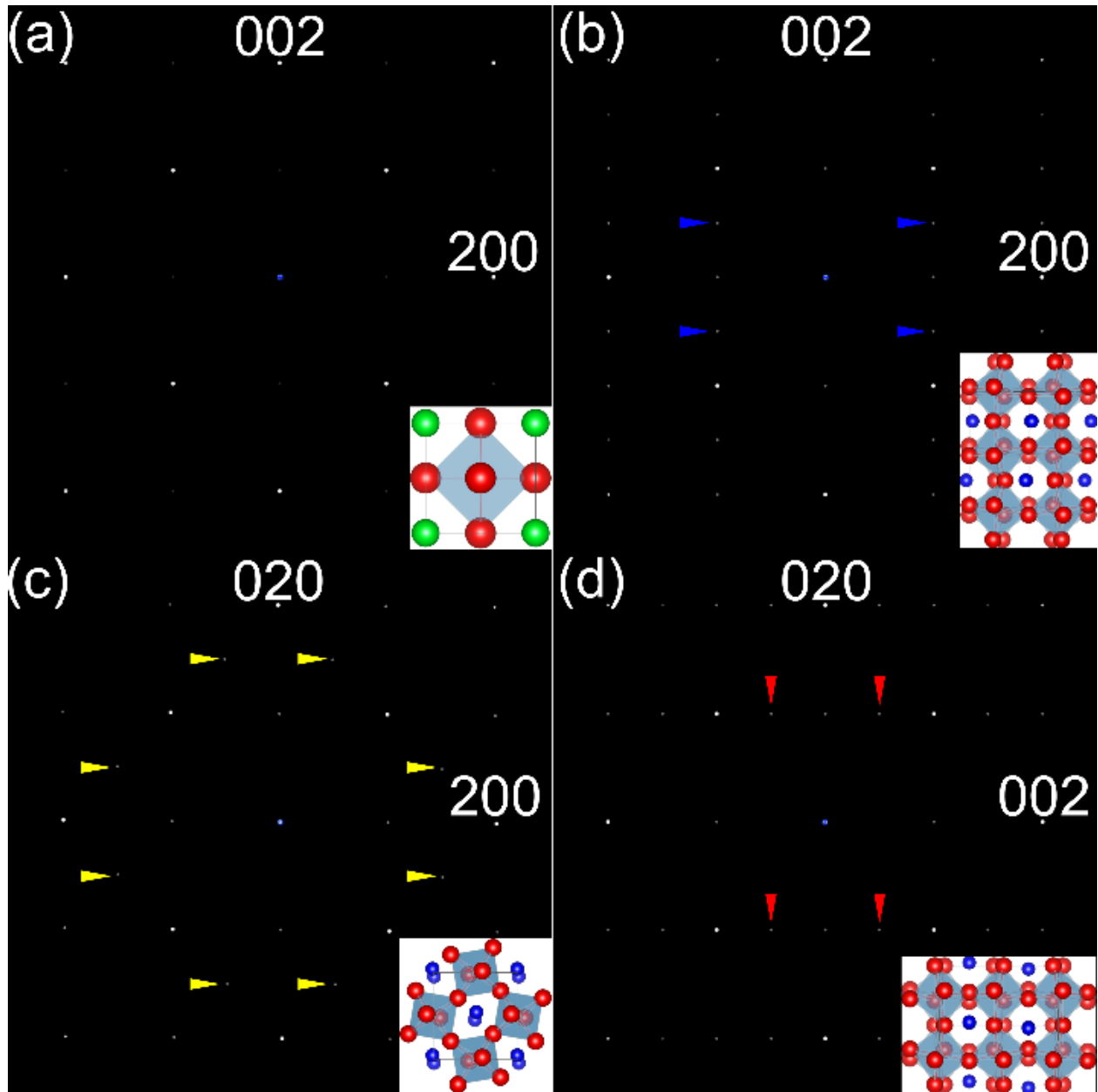


Figure S1. Simulated SADP for: (a) $Pm\bar{3}m$ and (b,d) $Pbnm$ along the out-of-phase tilt axis and (c) along the in-phase tilt axes. Blue, red, and yellow arrows indicate the same $\frac{1}{2}\{201\}_{pc}$, $\frac{1}{2}\{021\}_{pc}$, and $\frac{1}{2}\{130\}_{pc}$ ordered reflections, respectively, observed in the experimental SADP shown in Figure 1. Note that here the ordered reflections have different Miller indices that are based on the $Pbnm$ pseudo cubic axes while in Figure 1 the ordered reflections are labeled based on the STO axes aligned with the film geometry.

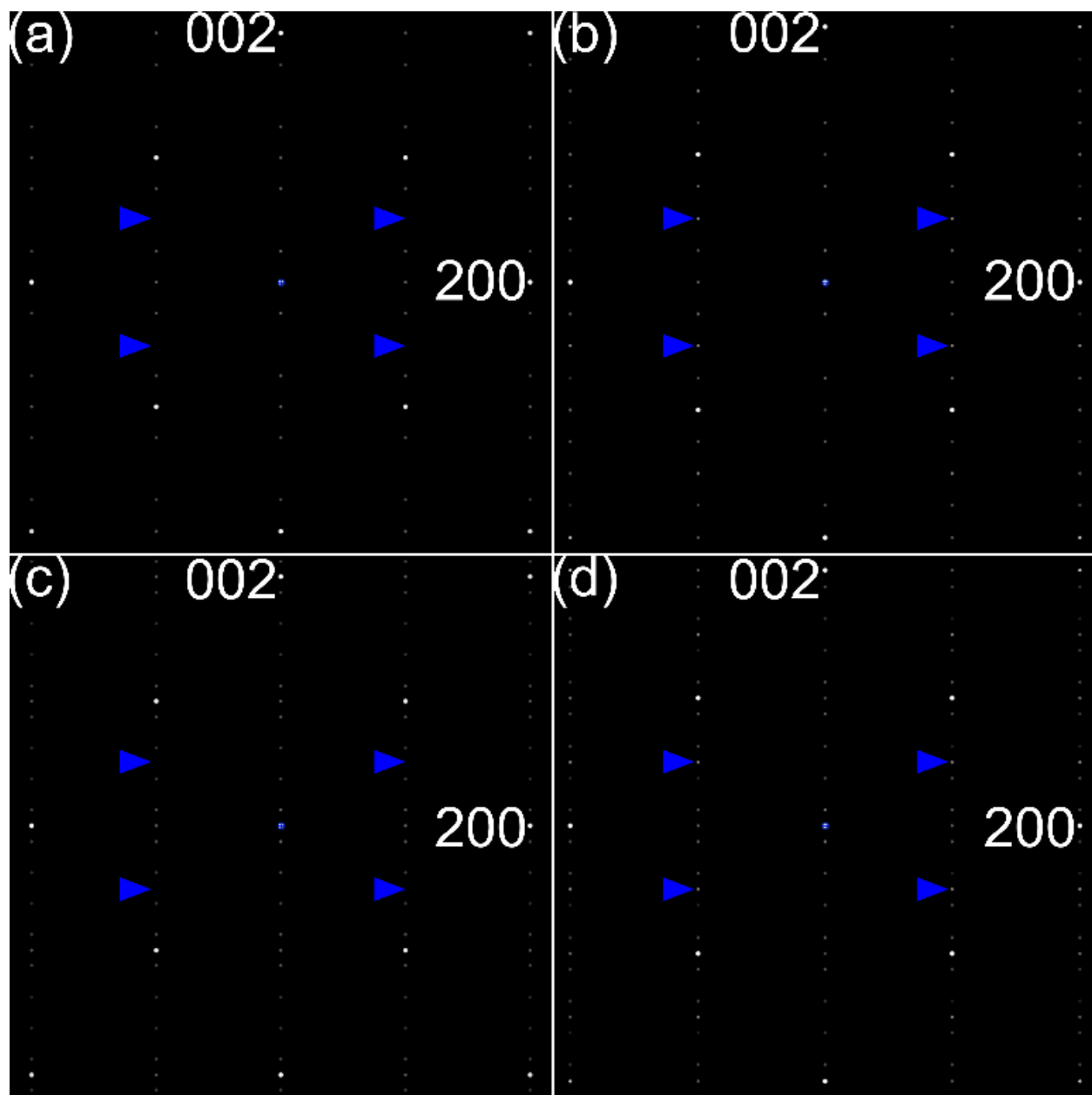


Figure S2. Simulated SADP for SL2 constructed from (a) four $\text{Pm}\bar{3}\text{m}$ and (b) two Pbnm unit-cells and SL4 constructed from (c) eight $\text{Pm}\bar{3}\text{m}$ and (d) four Pbnm unit-cells. Blue arrows indicate the absence of ordered reflections in $\text{Pm}\bar{3}\text{m}$ diffraction patterns and presence of $\frac{1}{2}\{201\}_{\text{pc}}$ type ordered reflection in Pbnm diffraction patterns.

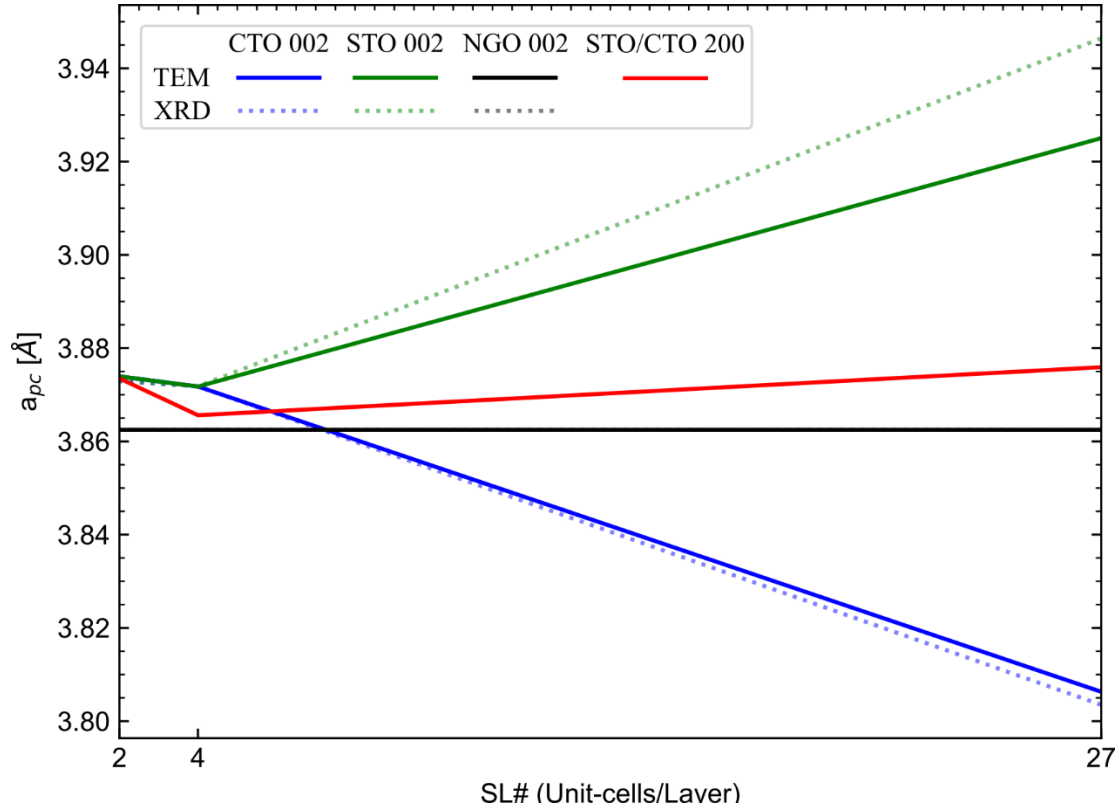


Figure S3. Calibrated lattice parameter calculated from the $(002)_{pc}$ Bragg peak using TEM SADP (solid) and x-ray diffraction (dotted) for CTO (blue), STO (green), and the NGO substrate (black). The in-plane lattice parameter for STO and CTO calculated from the $(200)_{pc}$ Bragg peak in a SADP is shown (red).

XRD was performed with a 2θ - ω scan geometry to determine the out-of-plane pseudocubic lattice constant. The NGO substrates $(002)_{pc}$ was used for alignment and the calculated lattice parameter showed minimal deviation between samples. It is assumed that the measured lattice parameter of the NGO substrate should be identical for all techniques and all samples. Therefore, all SADP and XRD measurements of STO, CTO, and NGO were scaled such that the NGO $(002)_{pc}$ lattice parameter equaled the average NGO $(002)_{pc}$ lattice parameter of the XRD scans. Lattice parameters were extracted from the SADP in Figure 1, and the scaled values are shown in Table S1. The lattice parameters calculated from XRD experiments are shown in Table S2. The

scaled lattice parameters from SADP and XRD are plotted together as a function of SL period in Figure S3.

Table S1. Scaled lattice parameters calculated from SADP in SL2, SL4, and SL27. Values are in Å.

	002 STO	CTO	NGO	200 STO/CTO
2	3.874			3.873
4	3.872			3.866
27	3.925	3.806		3.876

Table S2. Scaled lattice parameters calculated from XRD in SL2, SL4, and SL27. Values are in Å.

	STO	CTO	NGO
2	3.873		
4	3.872		3.862
27	3.804	3.946	

From the measured lattice parameters, it was found that the out-of-plane lattice parameter converged to a single STO/CTO value that was approximately the average of the two unrelaxed lattice parameters of SL27. This is the general theme observed in all crystallographic and vibrational structure analysis herein, that is, as the number of unit-cells in a layer decreases the structure converges to a singular, uniform, intermediate structure. The in-plane lattice parameter is different (but nearly equivalent) to the substrate in SL4 and 27. SL2 had in-plane lattice parameters like their out-of-plane lattice parameter and were larger than SL 4 and 27, indicating that the film in-plane lattice parameters are not determined by the substrate.

Convergent-beam electron diffraction patterns were acquired for each pixel of a line scan, known as scanning convergent-beam electron diffraction (SCBED), across the STO/CTO interfaces.

Ordered Laue zones in the atomic resolution SCBED allows mapping of octahedral tilt.³⁹ Line scans of a two, four, and twenty-seven unit-cell superlattice are shown in Figure S4.

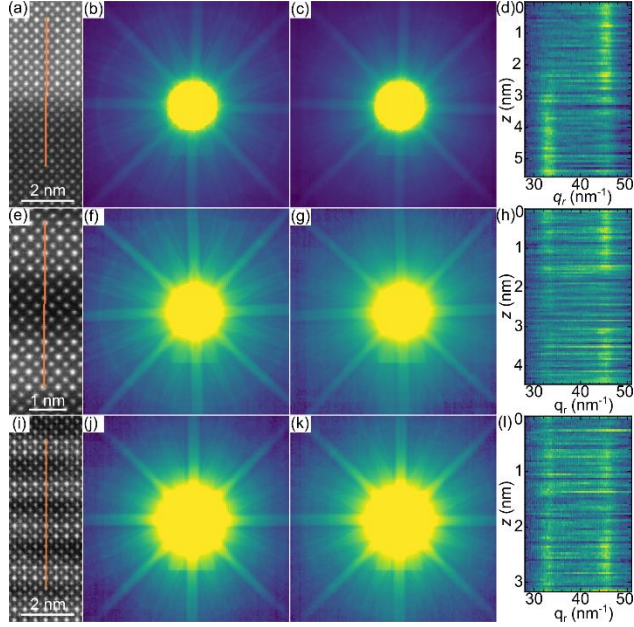


Figure S4. Scanning-CBED measurements from (a-d) SL27, (e-h) SL4, and (i-l) SL2. The position of line scans is indicated in the (a,e,i) ADF reference image. The PACBED pattern from the STO and CTO layers are shown in (b,f,j) and (c,g,k), respectively, show layer dependent fundamental and ordered Laue zones. (d,h,l) Background subtracted radially integrate CBED patterns show the existence of ordered reflections, indicative of octahedral tilting, as a function of position as the probe scanned across the superlattices.

The abrupt change in contrast of A-site atoms in the high-angle annular dark-field ((HA)ADF) signal shows the chemical abruptness of the superlattices. To visualize the relative difference in diffraction patterns taken from STO and CTO layers we compare the position averaged CBED (PACBED) from each layer, as shown in Figure S4(b,c). In the large period twenty-seven unit-cell superlattice the STO PACBED had a Laue zone corresponding to the intersection of the Ewald sphere with fundamental Bragg reflections of the $Pm\bar{3}m$ reciprocal lattice. The CTO PACBED had an identical fundamental Laue zone and an additional Laue zone, with half the radius of the fundamental, corresponding to the intersection of the Ewald sphere with half-integer ordered reflections appearing from TiO_6 tilting. The existence of tilting in CTO and not

in STO further supports the conclusion from SAED that STO and CTO are relaxed to their monolithic phases. When the number of unit-cells in a layer is reduced to four per layer the intensity of fundamental and ordered Laue zones in the CTO PACBED were much more similar, as shown in Figure S4(g). This could indicate some reduction in the octahedral tilt-angle, but in general shows that octahedral tilting still exists in CTO as expected from the SAED. With the decrease in layer thickness the STO PACBED now shows both a fundamental and ordered Laue zone much like CTO, as shown in Figure S4(f). Therefore, we conclude that the STO has inherited TiO_6 tilting from the CTO layers because of the reduced layer thickness. The inheritance of octahedral tilting persist with a further reduction to two unit-cells per layer and the comparable intensity of ordered and fundamental Laue zones is seen in both layers. The observed ordered reflections show that the STO layers are inheriting octahedral tilting and becoming adapting to the CTO crystal structure.

We know that the layers are changing and wanted to investigate more local changes. By radially integrating the CBED and subtracting a background power law the relative intensity of ordered and fundamental reflections at each pixel of a line scan is compared, as shown in Figure S4(d,h,l). In SL27 the intensity of the fundamental Laue zone is uniform in both CTO and STO layers and the intensity of the ordered Laue zone is uniform in the CTO layer showing that the structure of the layers is uniform, as shown in Figure S4(d). At the STO/CTO interface a transition region occurs over three atomic planes. In this transition region an ordered Laue zone appears in STO and gradually increases intensity as the probe entered the CTO. There is therefore a chemically abrupt and structurally diffuse interface that results from the coupling of STO and CTO layers, much like $\text{La}_{0.5}\text{Sr}_{0.5}\text{TiO}_3/\text{CTO}$ and $\text{NdGaO}_3/\text{CTO}$ interfaces.²² When the number of unit-cells is decreased to four or two unit-cells per layer, where the structurally

defined interface size is the same size as the chemically defined layers and octahedral tilting is present everywhere, the distinction between an interface region becomes less discernable. This could, in-part, be from relatively small contrast changes buried in noise, but implicates that the changes in ordered Laue zone intensity, indicating inheritance of octahedral tilting in STO and reduction of titling in CTO is from the overlapping structurally diffuse interfaces and the superlattice is transitioning to a system structurally defined by such interfaces.

S2 Supplemental: ADF and iDPC

In the STO layer of SL27 an in-phase tilt-angle of 1.84° and 2.69° STO was measured in the TiO_2 and AO planes, respectively, since no tilting is present and represents a bound to measurement error. In CTO out-of-phase tilt-angles of 10.04° and 10.32° in the TiO_2 and AO planes, respectively. In SL4 the quantified out-of-phase tilt-angle profile was sinusoidal with an average of 6.34° and 7.39° in the TiO_2 and AO planes, respectively, demonstrating that the layers tilts have accommodated to approach the mean or interface value observed in the larger-period SL27. In SL2 the tilt profile did not have any systematic tilt-angle related to the layer periodicity appearing “dephased” with a nearly constant tilt-angles of 7.138° and 6.096° in the AO and TiO_2 planes, respectively.

The relative proportion of layers and interfaces can be quantitatively assessed by comparing the volume fraction of interfaces, STO, and CTO defined by

$$V_{int} = \frac{1}{n-1} \quad (1a)$$

$$V_{STO} = V_{CTO} = \frac{n-2}{2(n-1)} \quad (1b)$$

In a large-period superlattice n is large so $V_{ATiO_3} \gg V_{Int}$. For a four unit-cell superlattice $V_{ATiO_3} = V_{Int}$ such that the interface is of equal importance to still existing layers. In the extreme of the two unit-cell superlattice $V_{ATiO_3}=0$ and $V_{Int}=1$ such that the entire superlattice is an ordered structure.

S3 Supplemental: DFT

In SL8 there is an asymmetry in tilt-angle gradient at the interface. The coupling extended further into the STO layer than into the CTO layer. The STO tilt-angle was also non-zero, unlike expected in bulk STO. The preferential increase in STO tilt-angles, relative to decreasing CTO angles, suggests that the O-Ti-O tilt mode is softer in STO. We cannot entirely rule out the influence of strain on this behavior.

Relaxed structures have lattice parameters different than the bulk STO and CTO lattice parameters. In SL8 the structure did not relax to the bulk like lattice parameters in the CTO and STO layers. A 1.8% compressive strain and 1.7% tensile strain is present in the STO and CTO layers, respectively, relative to bulk like phases.

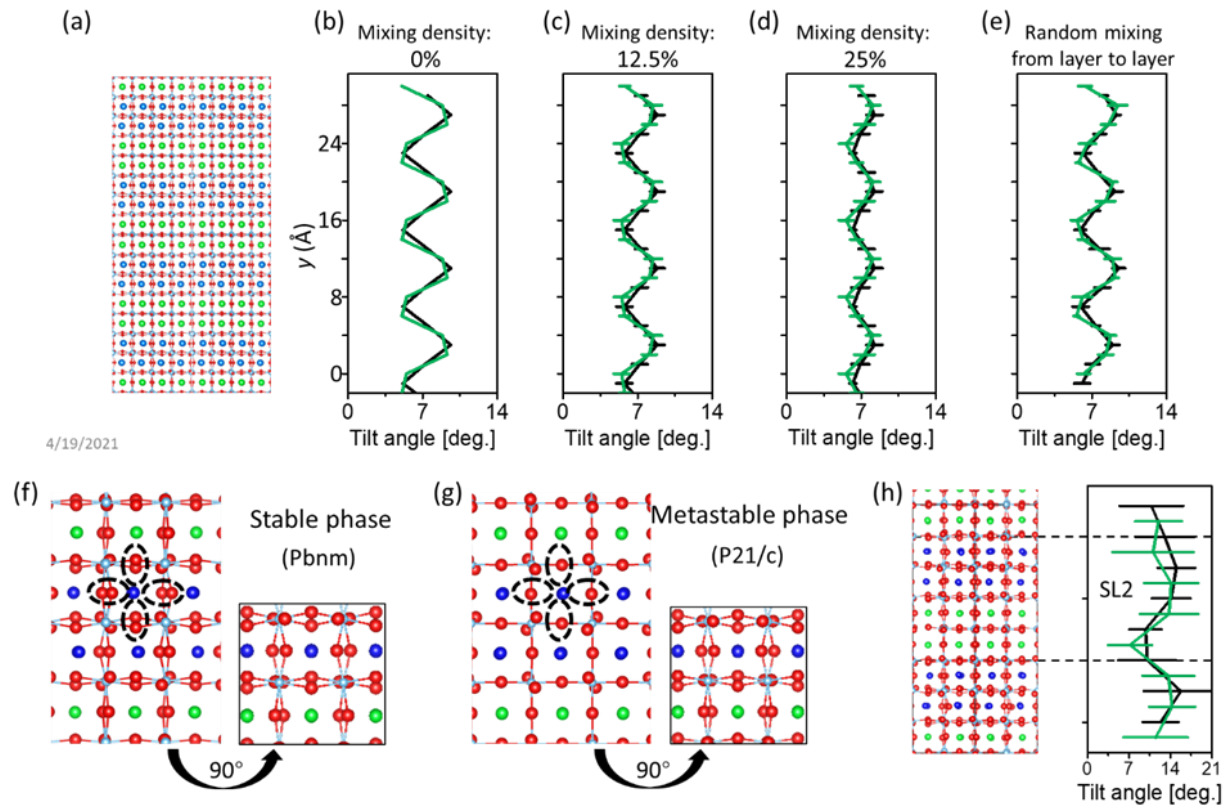


Figure S5. (a) Atomic model of SL2. (b-d) O-Ti-O tilt-angles as the uniform intermixing density changes from 0% to 25%. The y-axis scales are the same as in (a). (e) O-Ti-O tilt-angles when a 14.1% intermixing density is distributed nonuniformly in the layers. (f) Stable *Pbnm* phase of SL2. (g) Metastable phase of SL2 with *P21/c* symmetry. (h) O-Ti-O tilt-angles when oxygen vacancies are present, distributed randomly in the layers, with an overall density of $2.2 \times 10^{21} \text{ cm}^{-3}$ (this is a high density of vacancies, limited by computational costs)

Tilt-angles with different intermixing densities are calculated and shown in Figure S5(b-e). As the uniform intermixing density goes up, the tilt-angles are greatly decreased to an average value of 7° . Meanwhile, if the intermixing density is nonuniform (which is more likely experimentally), the tilt-angles not only decrease but also show a dephasing (Figure S5(e)). DFT calculations predict that SL2 may have a novel metastable phase with *P21/c* symmetry.

Comparing with the stable *Pbnm* phase, the metastable phase brings tiny lattices change to the crystal, namely a compression of 0.35% in *a*, and a stretch of 0.35% and 0.1% in *b* and *c*, respectively, and an increased total energy of 1.85 meV/atom. The small energy increase and

relationship between the structural space groups suggests that the existence of the metastable phase is highly possible, particularly at elevated temperatures. For the metastable phase, as shown in Figure S5(g), along the $[110]$ direction the horizontal and vertical O-Ti-O tilt-angles are zero for the higher symmetry-phase SL2, while along the $[1\bar{1}0]$ the tilts in the low-symmetry phase are still present. In such a case, measuring experimentally at a specific direction would obtain smaller tilt-angles than the expectation based on the stable state. The presence of rotational domains could lead to an averaging effect. All the above suggests that the presence of a temperature-dependent metastable phase and a small amount of intermixing may account for the constant angles in the experimental results of SL2. Moreover, oxygen vacancies are also considered in theoretical calculations. As shown in Figure S5(h), the existence of oxygen vacancies with a density of $2.2 \times 10^{21} \text{ cm}^{-3}$ cause the O-Ti-O tilt angles to increase significantly to over 14° , which is not the case with the experimental results. This result excludes the influence of oxygen vacancies in the experiments and confirms the high quality of the samples.

Additional discussion of Figure 2(b): Since the lattice parameters are optimized for the interfaces in the large-period calculations (e.g., SL8), there is always some strain on the STO and CTO layers. In our averaging method, we find very good agreement between the calculated SL27 phonon DOS and the experimentally measured EELS phonon spectra for SL27. By comparing the black curves with the orange curves in each model, we see that as the layer thickness decreases, the phonon DOS converges towards that of the interface curve, demonstrating the

dominance of the interface in thinner layer superlattices.

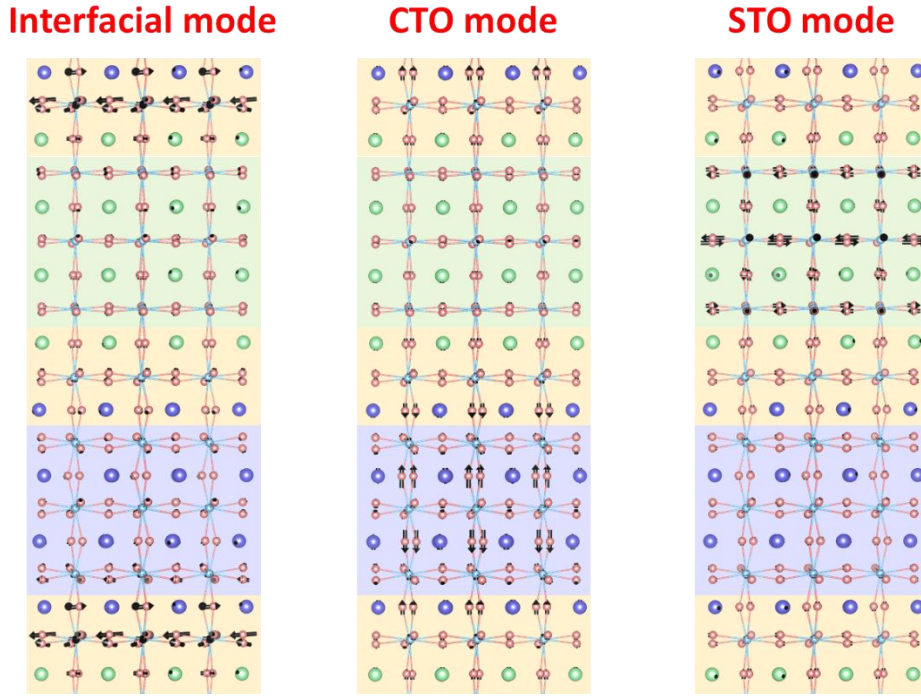


Figure S6. Eigenvectors for interface, CTO, and STO modes in SL4.

The eigenvectors for an interface mode, CTO layer mode, and STO layer mode are shown in Figure S6 to emphasize their spatial extent. These vectors can be envisioned as displacement vectors at one moment of time during vibrations. We find that the interface modes are localized to the three-atomic-plane-wide structurally diffuse interface. The STO and CTO layer modes are likewise localized within the layers. We can therefore use DFT to visualize the localization observed in vibrational EELS.

The phonon DOS discussed in the main text is Ti and O projected. This was done to emphasize the impact of octahedral rotations on the phonon DOS and because the EELS analysis energy range was >30 meV. For completeness, we show the remaining A-site projected phonon DOS in Figure S7. The Sr peak is lower energy than the Ca peak, because Sr is heavier. The Ca+Sr curve

in SL2 and SL4 are very similar suggesting that their A-site vibrational response is similar. Most importantly for our justification to neglect A-site bonding, thus emphasizing the impact of octahedral rotation, is that all A-site vibrational responses are less than 30 meV. The A-site vibrations only provide a continuously decaying background to the DOS above 30 meV.

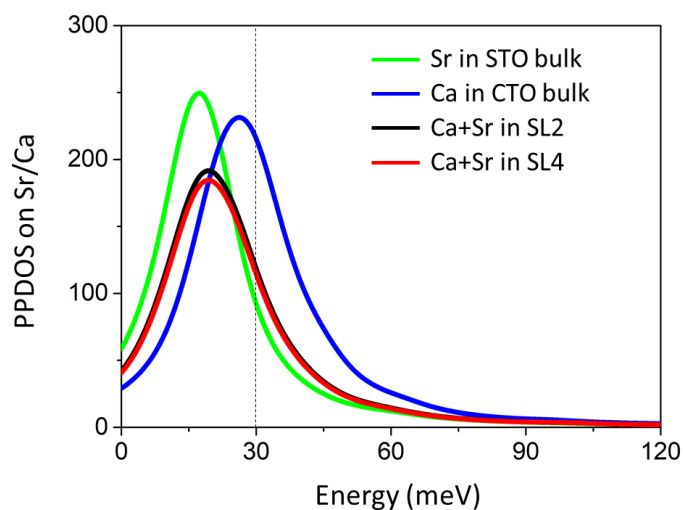


Figure S7. A-site projected phonon DOS.

S4 Supplemental: Vibrational EELS

ADF signal was collected simultaneously with EELS data was used to identify the position of STO and CTO layers and their interfaces. This was done by finding the inflection points in ADF signals via differentiation of the signal, peak finding, then manually removing irrelevant

positions. An example of interface assignment for an off-axis geometry acquired from SL27 is shown in Figure S8.

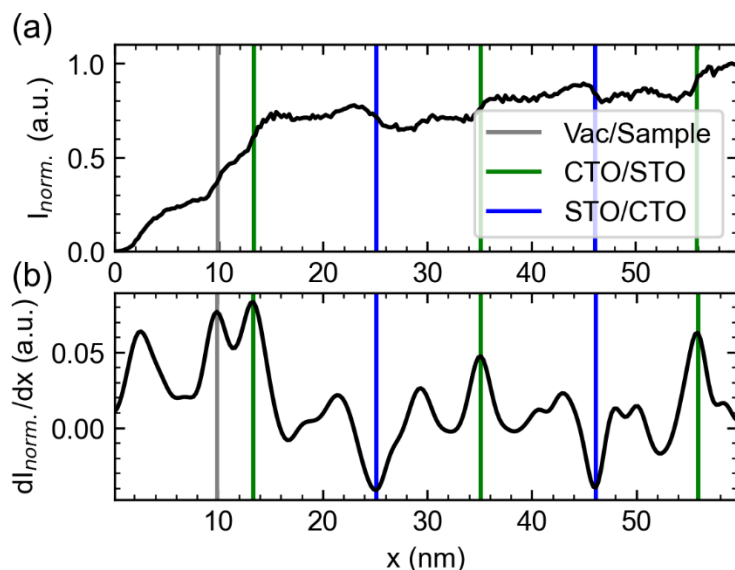


Figure S8. Example of interface assignment in SL27 off-axis signal.

In off-axis EELS line scans, ADF signals are asymmetric with Bragg reflections projecting onto the detector resulting in strain and diffraction contrast, which causes peaks in the ADF signal. An initial concern of qualitatively comparing the vibrational response of the layers and interfaces was that spatial differences in the differential scattering cross-section (with respect to \mathbf{q}) could easily be confused with shifting peaks leading to a misinterpretation of localized interface modes. One way to determine if the apparent changes are from a change in scattering cross-section or peak energy is to directly compare the spectra. The signal in each layer was averaged into a position averaged energy-loss spectra (PAELS) to reduce the number of spectra to compare and aid interpretation, as shown in Figure S9.

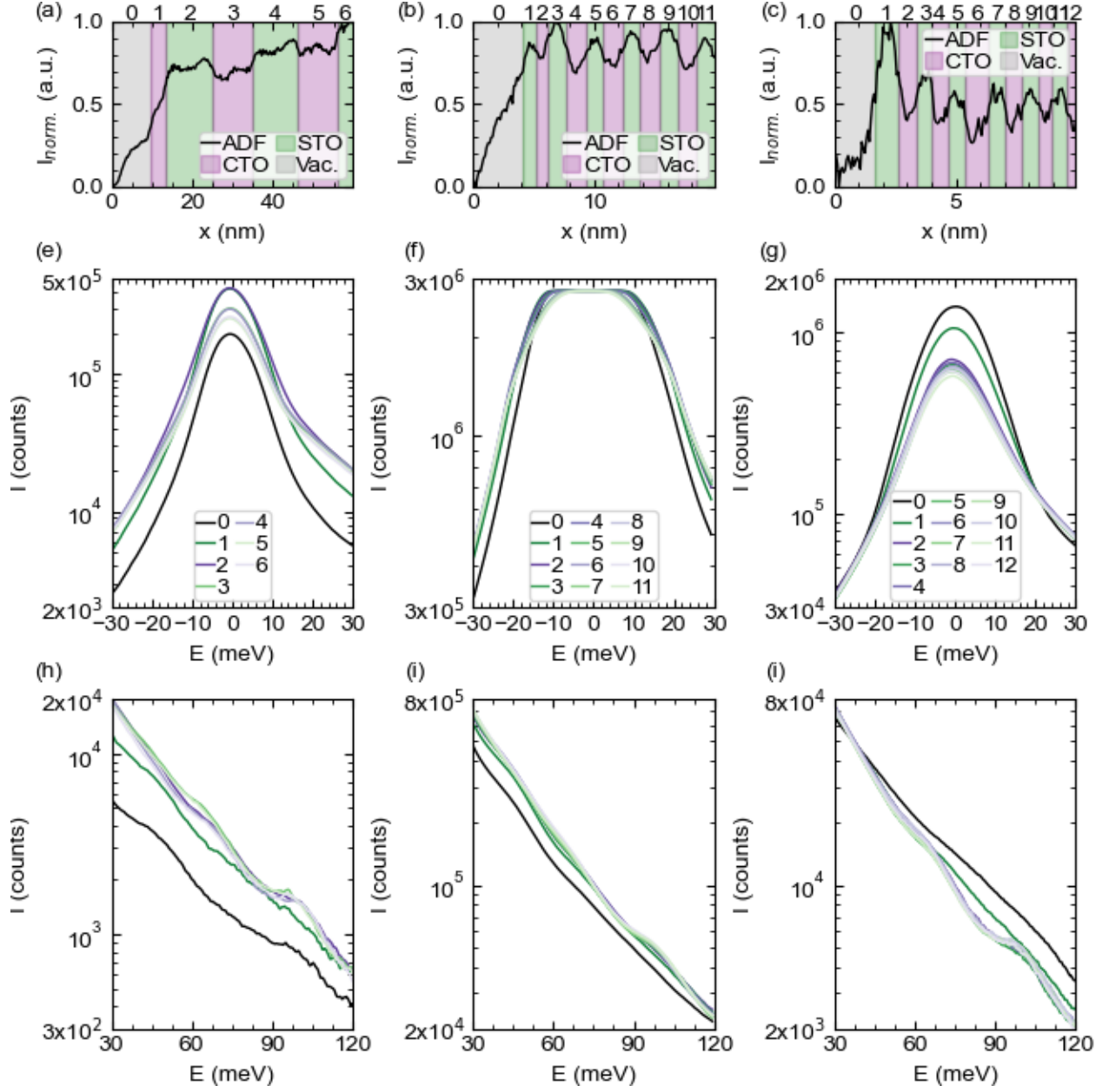


Figure S9. (a-c) ADF signal during the line scan with marker signifying defined layers in the off-axis geometry of (a,e,h) SL27, (b,f,i) SL4, and (c,g,i) SL2. PAELS of the (e-g) quasi-elastic peak and (h-i) loss region.

The quasi-elastic peak of the PAELS centered at $E=0$ meV is lowest when in vacuum for the off-axis geometry because localized quasi-elastic excitations are not excited. When the probe enters the material, phonons begin to inelastically scatter the incident electron and the quasi-elastic peak increases in intensity. One would expect that the quasi-elastic peak would then linearly

increase with thickness like the ADF signal, which is in-part a result of impact scattered phonons. Instead, the quasi-elastic response decreased with each successive period and each layer in a period had nearly the same magnitude quasi-elastic peak. The exact reason for this occurrence is not known, but the overall decrease in signal could be attributed increase scattering probability of other inelastic excitations, such as plasmons and core-states. Quickly after the probe is in the material the tails of the quasi-elastic peak converge to similar values allowing for the intensity of peaks on the tail of the quasi-elastic peak to be compared directly without considering the influence of the total inelastic differential cross-section. This is further shown by the vibrational response intensity and energy difference between STO and CTO (for example see the ~65 meV region) and similarity between each CTO or STO layer. The convergence was conservatively set at layer 3, 5, and 5, for SL27, SL4, and SL2, respectively.

We then include a finite interface width into the PAELS, defined as one ± 0.39 nm unit-cell, which is approximately one unit-cell on each side of the interface and contains the structurally diffuse interface measured in iDPC experiments. These newly defined layers and convergence point are used to form the layer average EELS in Figure 2 and Figure S10. Layer-averaged spectra in Figure 2 are shown as larger panels in Figure S10 to emphasize the small differences in peak energies, which are also listed in Table S3.

Table S3. Peak energies identified in the layer-averaged EELS spectra of Figure 2 and Figure S10. All energies are listed in meV.

	Peak 1			Peak 2			Peak 3		
	STO	Int.	CTO	STO	Int.	CTO	STO	Int.	CTO
SL27	40.1	45.5	46.2	66.7	66.1	63.3	100.3	98.6	96.8
SL4	45.3	45.9	45.9	69	68.2	67.3	98.2	96	95
SL2	36.2	37.3	38.5	64.3	63.5	63.1	98.8	98.1	98.8

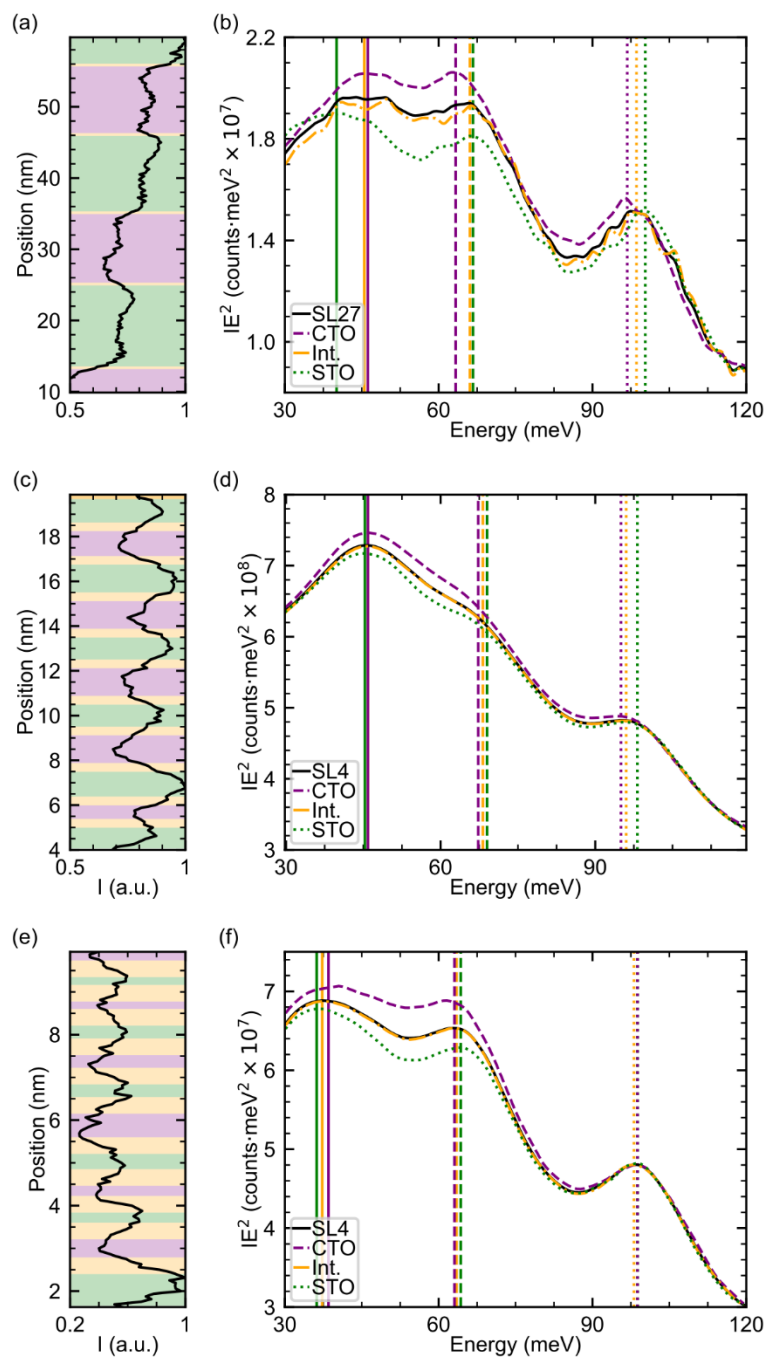


Figure S10. Monochromated STEM-EELS (b,d,f) layer-averaged spectra and (a,c,e) simultaneously acquired ADF signal.